Chapter 8

Early stages of evolution and the main sequence phase

In this and the following chapters, an account will be given of the evolution of stars as it follows from full-scale, detailed numerical calculations. Because the stellar evolution equations are highly non-linear, they have complicated solutions that cannot always be anticipated on the basis of fundamental principles. We must accept the fact that simple, intuitive explanations cannot always be given for the results that emerge from numerical computations. As a consequence, the account of stellar evolution that follows will be more descriptive and less analytical than previous chapters.

This chapter deals with early phases in the evolution of stars, as they evolve towards and during the main-sequence phase. We start the chapter with a very brief (and incomplete) overview of the formation of stars.

8.1 Star formation and pre-main sequence evolution

The process of star formation constitutes one of the main problems of modern astrophysics. Compared to our understanding of what happens *after* stars have formed out of the interstellar medium – that is, stellar evolution – star formation is a very ill-understood problem. No predictive theory of star formation exists, in other words: given certain initial conditions (e.g. the density and temperature distributions inside an interstellar cloud) it is as yet not possible to predict, for instance, the *star formation efficiency* (which fraction of the gas is turned into stars) and the resulting *initial mass function* (the spectrum and relative probability of stellar masses that are formed). We rely mostly on observations to answer these important questions.

This uncertainty might seem to pose a serious problem for studying stellar evolution: if we do not know how stars are formed, how can we hope to understand their evolution? The reason that stellar evolution is a much more quantitative and predictive branch of astrophysics than star formation was already alluded to in Chapter 6. Once a recently formed star settles into hydrostatic and thermal equilibrium on the main sequence, its structure is determined by the four structure equations and only depends on the initial composition. Therefore all the uncertain details of the formation process are wiped out by the time its nuclear evolution begins.

In the context of this course we can thus be very brief about star formation itself, as it has very little effect on the properties of stars themselves (at least as far as we are concerned with individual stars – it does of course have an important effect on stellar *populations*). Roughly, we can distinguish six stages in the star formation process, some of which are illustrated in Fig. 8.2.

1. Observations indicate that stars are formed out of molecular clouds, typically giant molecular

clouds with masses of order $10^5\,M_\odot$. These clouds have typical dimensions of $\sim$ 10 parsec, temperatures of $10 - 100$ K and densities of $10 - 300$ molecules/cm^3 (where the lowest temperatures pertain to the densest parts of the cloud). A certain fraction, about 1 %, of the cloud material is in the form of dust which makes the clouds very opaque to visual wavelengths. The clouds are in pressure equilibrium (hydrostatic equilibrium) with the surrounding interstellar medium.

Star formation starts when a perturbation (e.g. due to a shock wave originated by a nearby supernova explosion or a collision with another cloud) disturbs the pressure equilibrium and causes (part of) the cloud to collapse under its self-gravity. The condition for pressure equilibrium to be stable to such perturbations is that the mass involved should be less than a critical mass, the *Jeans mass* given by

$$M_{\rm J} \approx 10^5\,M_\odot \cdot (T/100\,{\rm K})^{1.5} n^{-0.5} \tag{8.1}$$

where n is the molecular number density in cm^{-3}. For typical values of T and n in molecular clouds $M_{\rm J} \sim 10^3 - 10^4\,M_\odot$. Cloud fragments with a mass exceeding the Jeans mass cannot maintain hydrostatic equilibrium and will undergo essentially free-fall collapse. Although the collapse is dynamical, the timescale $\tau_{\rm dyn} \propto \rho^{-1/2}$ (eq. 2.17) is of the order of millions of years because of the low densities involved. The cloud is transparent to far-infrared radiation and thus cools efficiently, so that the early stages of the collapse are *isothermal*.

2. As the density of the collapsing cloud increases, its Jeans mass decreases by eq. (8.1). The stability criterion within the cloud may now also be violated, so that the cloud starts to *fragment* into smaller pieces, each of which continues to collapse. The fragmentation process probably continues until the mass of the smallest fragments (dictated by the decreasing Jeans mass) is less than $0.1\,M_\odot$.

3. The increasing density of the collapsing cloud fragment eventually makes the gas *opaque* to infrared photons. As a result, radiation is trapped within the central part of the cloud, leading to heating and an increase in gas pressure. As a result the cloud core comes into hydrostatic equilibrium and the dynamical collapse is slowed to a quasi-static contraction. At this stage we may start to speak of a *protostar*.

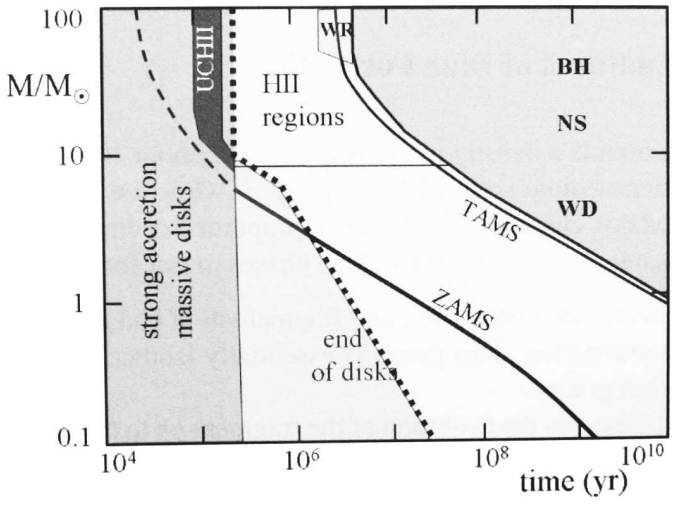

Figure 8.1. Timescales and properties of stars of mass M on the main sequence. Time along the abscissa is in logarithmic units to highlight the early phases, $t = 0$ corresponds to the formation of a hydrostatic core (stage 3 in the text). Initially the star is embedded in a massive accretion disk for $(1 - 2) \times 10^5$ years. In low-mass stars the disk disappears before the star settles on the zero-age main sequence (ZAMS). Massive stars reach the ZAMS while still undergoing strong accretion. These stars ionize their surroundings and excite an HII region around themselves. TAMS stands for terminal-age main sequence.

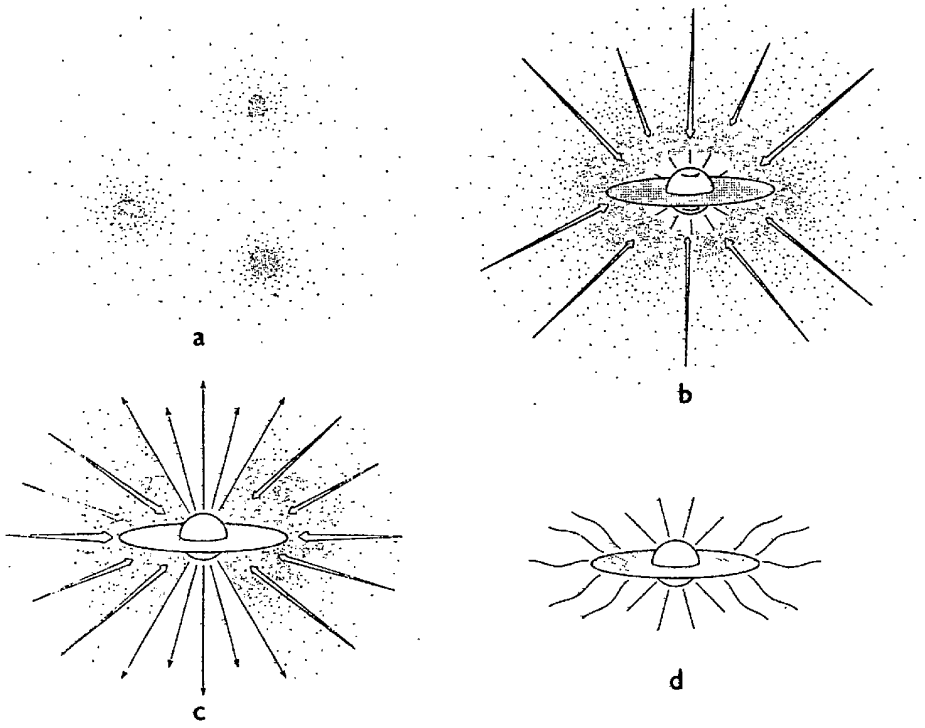

Figure 8.2. Cartoon illustrating four stages in the star formation process, according to Shu (1987). (a) Protostellar cores form within a molecular cloud as a result of fragmentation. (b) A protostar builds up by accreting from the surrounding, infalling gas. Due to conservation of angular momentum within the protostellar nebula, the accretion occurs via a disk. (c) Bipolar flows break out along the rotation axis where the gas density is lowest, powered by the accretion luminosity. These outflows are seen around low-mass protostars known as T Tauri stars. Finally, in (d) the surrounding nebular material is swept away and the newly formed pre-main sequence star becomes visible (still with a remnant accretion disk around it).

4. The surrounding gas keeps falling onto the protostellar core, so that the next phase is dominated by *accretion*. Since the contracting clouds contain a substantial amount of angular momentum, the infalling gas forms an accretion disk around the protostar. These *accretion disks* are a ubiquitous feature of the star formation process and are observed around most very young stars (mostly at infrared and sub-millimeter wavelengths).

   The accretion of gas generates gravitational energy, part of which goes into further heating of the core and part of which is radiated away, providing the luminosity of the protostar, so that

$$L \sim L_{\rm acc} = \frac{GM\dot{M}}{2R} \tag{8.2}$$

   where M and R are the mass and radius of the core and $\dot{M}$ is the mass accretion rate. The factor $\frac{1}{2}$originates from the fact that half of the potential energy is dissipated in the accretion disk. Meanwhile he core heats up almost adiabatically since the accretion timescale $\tau_{\rm acc} = M/\dot{M}$ is much smaller than the thermal timescale $\tau_{\rm KH}$.

5. The gas initially consists of molecular hydrogen and behaves like an ideal gas, such that $\gamma_{\rm ad} > \frac{4}{3}$ and the protostellar core is dynamically stable. When the core temperature reaches $\sim 2000\,{\rm K}$ molecular hydrogen starts to dissociate, which is analogous to ionization and leads to a strong

increase of the specific heat and a decrease of $\gamma_{\rm ad}$ below the critical value of $\frac{4}{3}$ (Sect. 3.5). Hydrostatic equilibrium is no longer possible and a renewed phase of *dynamical collapse* follows, during which the gravitational energy release is absorbed by the dissociating molecules without a significant rise in temperature. When H_2 is completely dissociated into atomic hydrogen HE is restored and the temperature rises again. Somewhat later, further dynamical collapse phases follow when first H and then He are ionized at $\sim 10^4$ K. When ionization of the protostar is complete it settles back into hydrostatic equilibrium at a much reduced radius (see below).

6. Finally, the accretion slows down and eventually stops and the protostar is revealed as a *pre-main sequence star*. Its luminosity is now provided by gravitational contraction and, according to the virial theorem, its internal temperature rises as $T \propto M^{2/3}\rho^{1/3}$ (Chapter 7). The surface cools and a temperature gradient builds up, transporting heat outwards. Further evolution takes place on the thermal timescale $\tau_{\rm KH}$.

A rough estimate of the radius of a protostar after the dynamical collapse phase can be obtained by assuming that all gravitational energy released during the collapse was absorbed in dissociation of molecular hydrogen (requiring $\chi_{\rm H_2} = 4.5\,$eV per H_2 molecule) and ionization of hydrogen ($\chi_{\rm H} = 13.6\,$eV) and helium ($\chi_{\rm He} = 79\,$eV). Taking the collapse to start from infinity (since the final radius will be much smaller than the initial one) we can write

$$\frac{GM^2}{R_{\rm p}} \approx \frac{M}{m_{\rm u}}\left(\frac{X}{2}\chi_{\rm H_2} + X\chi_{\rm H} + \frac{Y}{4}\chi_{\rm He}\right) \tag{8.3}$$

which gives, taking $X \approx 0.7$ and $Y = 1 - X$,

$$\frac{R_{\rm p}}{R_\odot} \approx 120\frac{M}{M_\odot} \tag{8.4}$$

The average internal temperature can be estimated from the virial theorem (Sect. 2.3), since the protostar is in hydrostatic equilibrium,

$$\bar{T} \approx \tfrac{1}{3}\frac{\mu}{\mathcal{R}}\frac{GM}{R_{\rm p}} \approx 6\times 10^4\,{\rm K}, \tag{8.5}$$

independent of its mass. At these low temperatures the opacity is very high, rendering radiative transport inefficient and making the protostar convective throughout. The properties of such *fully convective stars* must be examined more closely.

8.1.1 Fully convective stars: the Hayashi line

We have seen in Sect. 6.2.3 that as the effective temperature of a star decreases the convective envelope gets deeper, occupying a larger and larger part of the mass. If $T_{\rm eff}$ is small enough stars can therefore become completely convective. In that case, as we derived in Sect. 4.5.2, energy transport is very efficient throughout the interior of the star, and a tiny superadiabaticity $\nabla - \nabla_{\rm ad}$ is sufficient to transport a very large energy flux. The structure of such a star can be said to be *adiabatic*, meaning that the temperature stratification (the variation of temperature with depth) as measured by $\nabla = d\log T/d\log P$ is equal to $\nabla_{\rm ad}$. Since an almost arbitrarily high energy flux can be carried by such a temperature gradient, the *luminosity* of a fully convective star is practically *independent of its structure* – unlike for a star in radiative equilibrium, for which the luminosity is strongly linked to the temperature gradient.

It turns out that:

Fully convective stars of a given mass occupy an almost vertical line in the H-R diagram (i.e. with $T_{\rm eff} \approx$ constant). This line is known as the *Hayashi line*. The region to the right of the Hayashi line in the HRD (i.e. at lower effective temperatures) is a *forbidden region* for stars in hydrostatic equilibrium. On the other hand, stars to the left of the Hayashi line (at higher $T_{\rm eff}$) cannot be fully convective but must have some portion of their interior in radiative equilibrium.

Since these results are important, not only for pre-main sequence stars but also for later phases of evolution, we will do a simplified derivation of the properties of the Hayashi line in order to make the above-mentioned results plausible.

Simple derivation of the Hayashi line

For any luminosity L, the interior structure is given by $\nabla = \nabla_{\rm ad}$. For an ideal gas we have a constant $\nabla_{\rm ad} = 0.4$, if we ignore the variation of $\nabla_{\rm ad}$ in partial ionization zones. We also ignore the non-zero superadiabaticity of ∇ in the sub-photospheric layers (Sect. 4.5.2). The temperature stratification throughout the interior can then be described by a power law $T \propto P^{0.4}$, which describes a polytrope of index $n = \frac{3}{2}$ as can be seen by eliminating T from this expression using the ideal gas law. We can thus write

$$P = K\rho^{5/3}.$$

The constant K for a polytrope of index n is related to the mass and radius by

$$K = C_n G M^{\frac{n-1}{n}} R^{\frac{3-n}{n}} \qquad \text{with} \qquad C_n = \frac{1}{n+1}\left(\frac{4\pi}{{z_n}^{3-n}{\theta_n}^{n-1}}\right)^{1/n}$$

(as can be seen by combining eqs. 7 and 8 in the practicum manual *Polytropic stellar models*; see also K&W section 19.4). For our fully convective star with $n = \frac{3}{2}$ we have $C_{3/2} = 0.4243$ and therefore

$$K = 0.4243\, G M^{1/3} R. \tag{8.6}$$

Since the luminosity of a fully convective star is not determined by its interior structure, it must follow from the conditions (in particular the *opacity*) in the thin radiative layer from which photons escape, the photosphere. We approximate the photosphere by a spherical surface of negligible thickness, where we assume the photospheric boundary conditions (6.9) to hold. Writing the pressure, density and opacity in the photosphere (at $r = R$) as P_R, ρ_R and κ_R and the photospheric temperature as $T_{\rm eff}$, we can write the boundary conditions as

$$\kappa_R P_R = \frac{2}{3}\frac{GM}{R^2}, \tag{8.7}$$

$$L = 4\pi R^2 \sigma T_{\rm eff}^4, \tag{8.8}$$

and we assume a power-law dependence of κ on ρ and T so that

$$\kappa_R = \kappa_0 {\rho_R}^a T_{\rm eff}^b. \tag{8.9}$$

The equation of state in the photospheric layer is

$$P_R = \frac{\mathcal{R}}{\mu}\rho_R T_{\rm eff}. \tag{8.10}$$

The interior, polytropic structure must match the conditions in the photosphere so that (using eq. 8.6)

$$P_R = 0.4243\, G M^{1/3} R {\rho_R}^{5/3}. \tag{8.11}$$

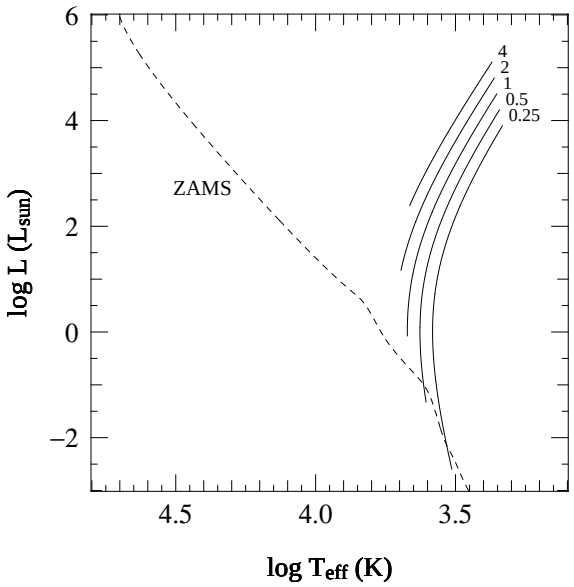

Figure 8.3. The position of the Hayashi lines in the H-R diagram for masses $M = 0.25$, 0.5, 1.0, 2.0 and 4.0 $M_\odot$ as indicated. The lines are analytic fits to detailed models computed for composition $X = 0.7, Z = 0.02$. The zero-age main sequence (ZAMS) for the same composition is shown as a dashed line, for comparison.
Note that the Hayashi lines do not have a constant slope, as expected from the simple analysis, but have a convex shape where the constant A (eq. 8.12) changes sign and becomes negative for high luminosities. The main reason is our neglect of ionization zones (where $\nabla_{\rm ad} < 0.4$) and the non-zero superadiabaticity in the outer layers, both of which have a larger effect in more extended stars.

For a given mass M, eqs. (8.7-8.11) constitute five equations for six unknowns, P_R, ρ_R, κ_R, $T_{\rm eff}$, L and R. The solution thus always contains one free parameter, that is, the solution is a relation between two quantities, say L and $T_{\rm eff}$. This relation describes the *Hayashi line* for a fully convective star of mass M.

Since we have assumed power-law expressions in all the above equations, the set of equations can be solved straightforwardly (involving some tedious algebra) to give a power-law relation between L and $T_{\rm eff}$ after eliminating all other unknowns. The solution can be written as

$$\log T_{\rm eff} = A \log L + B \log M + C \tag{8.12}$$

where the constants A and B depend on the exponents a and b in the assumed expression for the opacity (8.9),

$$A = \frac{\frac{3}{2}a - \frac{1}{2}}{9a + 2b + 3} \qquad \text{and} \qquad B = \frac{a + 3}{9a + 2b + 3}. \tag{8.13}$$

Therefore the shape of the Hayashi line in the HRD is determined by how the opacity in the photosphere depends on ρ and T. Since fully convective stars have very cool photospheres, the opacity is mainly given by H^- absorption (Sect. 4.3) which increases strongly with temperature. Very roughly, $a \approx 1$ and $b \gtrsim 4$ in the the relevant range of density and temperature, which gives $A \lesssim 0.05$ and $B \lesssim 0.2$. Therefore (see Fig. 8.3)

- for a certain mass the Hayashi line is a very steep, almost vertical line in the HRD,
- the position of the Hayashi line depends on the mass, being located at higher $T_{\rm eff}$ for higher mass.

The forbidden region in the H-R diagram

Consider models in the neighbourhood of the Hayashi line in the H-R diagram for a star of mass M. These models cannot have $\nabla = \nabla_{\rm ad}$ throughout, because otherwise they would be *on* the Hayashi line. Defining $\overline{\nabla}$ as the average value of $d \log T / d \log P$ over the entire star, models on either side of the Hayashi line (at lower or higher $T_{\rm eff}$) have either $\overline{\nabla} > \nabla_{\rm ad}$ or $\overline{\nabla} < \nabla_{\rm ad}$. It turns out (after more tedious

analysis of the above equations and their dependence on polytropic index n) that models with $\bar{\nabla} < \nabla_{\rm ad}$ lie at higher $T_{\rm eff}$ than the Hayashi line (to its left in the HRD) while models with $\bar{\nabla} > \nabla_{\rm ad}$ lie at lower $T_{\rm eff}$ (to the right in the HRD).

Now consider the significance of $\bar{\nabla} \neq \nabla_{\rm ad}$. If on average $\bar{\nabla} < \nabla_{\rm ad}$ then some part of the star must have $\nabla < \nabla_{\rm ad}$, that is, a portion of the star must be radiative. Since models in the vicinity of the Hayashi line still have cool outer layers with high opacity, the radiative part must lie in the deep interior. Therefore stars located (somewhat) to the *left* of the Hayashi line have radiative cores surrounded by convective envelopes (if they are far to the left, they can of course be completely radiative).

On the other hand, if $\bar{\nabla} > \nabla_{\rm ad}$ then a significant part of the star must have a *superadiabatic* temperature gradient (that is to say, apart from the outermost layers which are always superadiabatic). According to the analysis of Sect. 4.5.2, a significantly positive $\nabla - \nabla_{\rm ad}$ will give rise to a very large convective energy flux, far exceeding normal stellar luminosities. Such a large energy flux very rapidly (on a dynamical timescale) transports heat outwards, thereby decreasing the temperature gradient in the superadiabatic region until $\nabla = \nabla_{\rm ad}$ again. This restructuring of the star will quickly bring it back to the Hayashi line. Therefore the region to the right of the Hayashi line, with $T_{\rm eff} < T_{\rm eff,HL}$, is a *forbidden region* for any star in hydrostatic equilibrium.

8.1.2 Pre-main-sequence contraction

As a newly formed star emerges from the dynamical collapse phase it settles on the Hayashi line appropriate for its mass, with a radius roughly given by eq. (8.4). From this moment on we speak of the *pre-main sequence* phase of evolution. The pre-main sequence (PMS) star radiates at a luminosity determined by its radius on the Hayashi line. Since it is still too cool for nuclear burning, the energy source for its luminosity is gravitational contraction. As dictated by the virial theorem, this leads to an increase of its internal temperature. As long as the opacity remains high and the PMS star remains fully convective, it contracts along its Hayashi line and thus its luminosity decreases. Since fully convective stars are accurately described by $n = 1.5$ polytropes, this phase of contraction is indeed homologous to a very high degree! Thus the central temperature increases as $T_c \propto \rho_c^{1/3} \propto 1/R$.

As the internal temperature rises the opacity (and thus $\nabla_{\rm rad}$) decreases, until at some point $\nabla_{\rm rad} < \nabla_{\rm ad}$ in the central parts of the star and a radiative core develops. The PMS star then moves to the left in the H-R diagram, evolving away from the Hayashi line towards higher $T_{\rm eff}$ (see Fig. 8.4). As it keeps on contracting the extent of its convective envelope decreases and its radiative core grows in mass. (This phase of contraction is no longer homologous, because the density distribution must adapt itself to the radiative structure.) The luminosity no longer decreases but increases somewhat. Once the star is mainly radiative further contraction is again close to homologous. The luminosity is now related to the temperature gradient and mostly determined by the mass of the protostar (see Sect. 6.4.2). This explains why PMS stars of larger mass turn away from the Hayashi line at a higher luminosity than low-mass stars, and why their luminosity remains roughly constant afterward.

Contraction continues, as dictated by the virial theorem, until the central temperature becomes high enough for nuclear fusion reactions. Once the energy generated by hydrogen fusion compensates for the energy loss at the surface, the star stops contracting and settles on the *zero-age main sequence* (ZAMS) if its mass is above the hydrogen burning limit of 0.08 $M_\odot$ (see Chapter 7). Since the nuclear energy source is much more concentrated towards the centre than the gravitational energy released by overall contraction, the transition from contraction to hydrogen burning again requires a (non-homologous) rearrangement of the internal structure.

Before thermal equilibrium on the ZAMS is reached, however, several nuclear reactions have already set in. In particular, a small quantity of *deuterium* is present in the interstellar gas out of

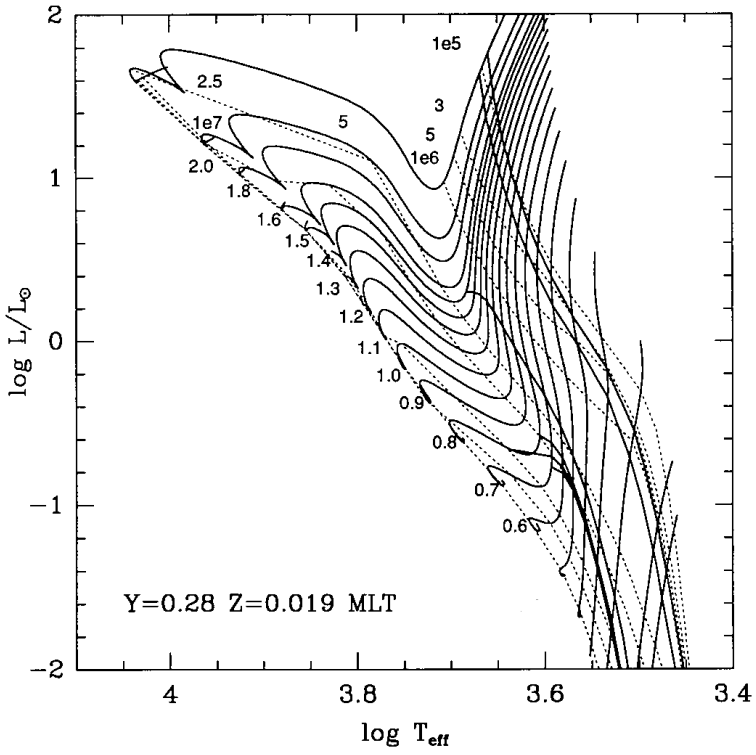

Figure 8.4. Pre-main-sequence evolution tracks for $0.3 - 2.5\,M_\odot$, according to the calculations of D'Antona & Mazzitelli (1994). The dotted lines are isochrones, connecting points on the tracks with the same age (between $t = 10^5$ yrs and 10^7 yrs, as indicated). Also indicated as solid lines that cross the tracks are the approximate locations of deuterium burning (between the upper two lines, near the $t \sim 10^5$ yr isochrone) and lithium burning (crossing the tracks at lower luminosity, at $t > 10^6$ yr).

which stars form, with a mass fraction $\sim 10^{-5}$. Deuterium is a very fragile nucleus that reacts easily with normal hydrogen ($^2\mathrm{H} + {}^1\mathrm{H} \rightarrow {}^3\mathrm{He} + \gamma$, the second reaction in the pp chain). This reaction destroys all deuterium present in the star when $T \approx 1.0 \times 10^6$ K, while the protostar is still on the Hayashi line. The energy produced (5.5 MeV per reaction) is large enough to halt the contraction of the PMS star for a few times 10^5 yr. (A similar but much smaller effect happens somewhat later at higher T when the initially present lithium, with mass fraction $\lesssim 10^{-8}$, is depleted). Furthermore, the $^{12}\mathrm{C}(\mathrm{p},\gamma)^{13}\mathrm{N}$ reaction is already activated at a temperature below that of the full CNO-cycle, due to the relatively large initial ^{12}C abundance compared to the equilibrium CNO abundances. Thus almost all ^{12}C is converted into ^{14}N before the ZAMS is reached. The energy produced in this way also halts the contraction temporarily and gives rise to the wiggles in the evolution tracks just above the ZAMS location in Fig, 8.4. Note that this occurs even in low-mass stars, $\lesssim 1\,M_\odot$, even though the pp chain takes over the energy production on the main sequence in these stars once CN equilibrium is achieved (see Sect. 8.2).

Finally, the time taken for a protostar to reach the ZAMS depends on its mass. This time is basically the Kelvin-Helmholtz contraction timescale (eq. 2.34). Since contraction is slowest when both R and L are small, the pre-main sequence lifetime is dominated by the final stages of contraction, when the star is already close to the ZAMS. We can therefore estimate the PMS lifetime by putting ZAMS values into eq. (2.34) which yields $\tau_{\mathrm{PMS}} \approx 10^7 (M/M_\odot)^{-2.5}$ yr. Thus massive protostars reach the ZAMS much earlier than lower-mass stars (and the term 'zero-age' main sequence is somewhat misleading in this context, although it hardly makes a difference to the total lifetime of a star). Indeed in young star clusters (e.g. the Pleiades) only the massive stars have reached the main sequence while low-mass stars still lie above and to the right of it.

8.2 The zero-age main sequence

Stars on the zero-age main sequence are (nearly) homogeneous in composition and are in complete (hydrostatic and thermal) equilibrium. Detailed models of ZAMS stars can be computed by solving the four differential equations for stellar structure numerically. It is instructive to compare the properties of such models to the simple main-sequence homology relations derived in Sect. 6.4.

From the homology relations we expect a homogeneous, radiative star in hydrostatic and thermal equilibrium with constant opacity and an ideal-gas equation of state to follow a mass-luminosity and mass-radius relation (6.32 and 6.36),

$$L \propto \mu^4 M^3, \qquad R \propto \mu^{\frac{\nu-4}{\nu+3}} M^{\frac{\nu-1}{\nu+3}}.$$

These relations are shown as dashed lines in Fig. 8.5, where they are compared to observed stars with accurately measured M, L and R (see Chapter 1) and to detailed ZAMS models. The mass-radius homology relation depends on the temperature sensitivity (ν) of the energy generation rate, and is thus expected to be different for stars in which the pp chain dominates ($\nu \approx 4$, $R \propto M^{0.43}$) and stars dominated by the CNO cycle ($\nu \approx 18$, $R \propto \mu^{0.67} M^{0.81}$, as was assumed in Fig. 8.5).

Homology predicts the qualitative behaviour rather well, that is, a steep L-M relation and a much shallower R-M relation. However, it is not quantitatively accurate and it cannot account for the changes in slope ($d \log L / d \log M$ and $d \log R / d \log M$) of the relations. This was not to be expected, given the simplifying assumptions made in deriving the homology relations. The slope of the L-M relation is shallower than the homology value of 3 for masses below $1\,M_\odot$, because such stars have large convective envelopes (as illustrated in Sect. 4.5; see also Sect. 8.2.2 below). The slope is significantly steeper than 3 for masses between 1 and 10 $M_\odot$: in these stars the main opacity source is free-free and bound-free absorption, which increases outward rather than being constant through the star. In very massive stars, radiation pressure is important which results in flattening the L-M relation.

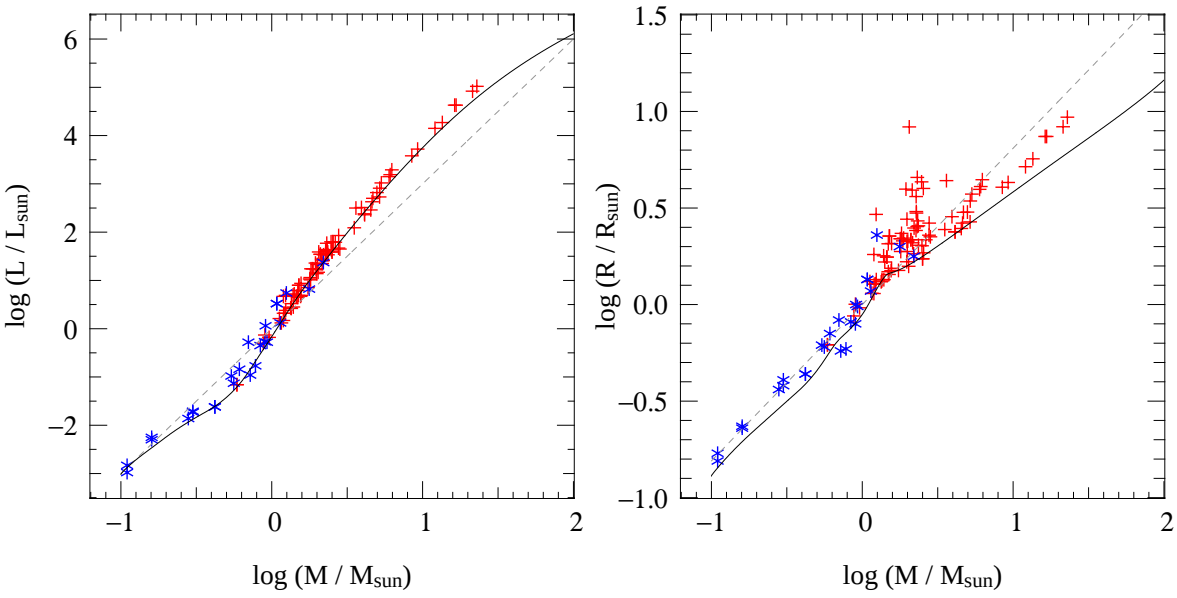

Figure 8.5. ZAMS mass-luminosity (left) and mass-radius (right) relations from detailed structure models with $X = 0.7, Z = 0.02$ (solid lines) and from homology relations scaled to solar values (dashed lines). For the radius homology relation, a value $\nu = 18$ appropriate for the CNO cycle was assumed (giving $R \propto M^{0.81}$); this does not apply to $M < 1\,M_\odot$ so the lower part should be disregarded. Symbols indicate components of double-lined eclipsing binaries with accurately measured M, R and L, most of which are MS stars.

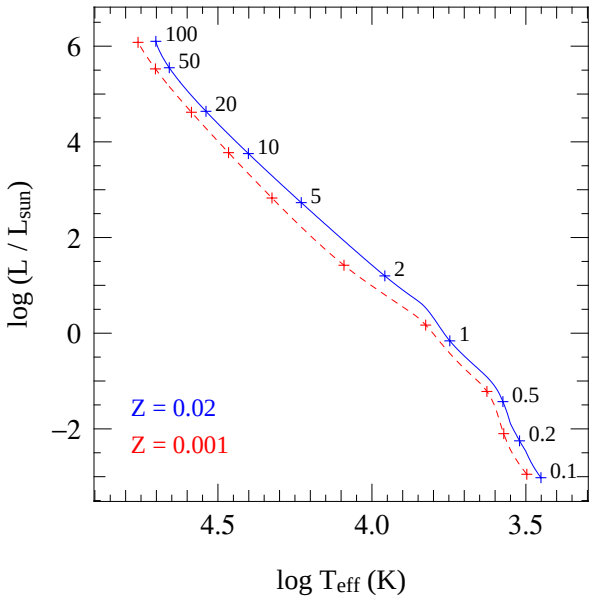

Figure 8.6. The location of the zero-age main sequence in the Hertzsprung-Russell diagram for homogeneous, detailed stellar models with $X = 0.7, Z = 0.02$ (blue solid line) and with $X = 0.757, Z = 0.001$ (red dashed line). Plus symbols indicate models for specific masses (in units of $M_\odot$). ZAMS models for metal-poor stars are hotter and have smaller radii. Relatively low-mass stars at low metallicity are also more luminous than their metal-rich counterparts.

The reasons for the changes in $d \log R / d \log M$ are similar. Note that for low masses we should have used the homology relation for the pp chain (for reasons explained in Sect. 8.2.1 below), which has a *smaller* slope – the opposite of what is seen in the detailed ZAMS models. The occurrence of convective regions (see Sect. 8.2.2) is the main reason for this non-homologous behaviour.

The detailed ZAMS models do reproduce the observed stellar luminosities quite well. The models trace the lower boundary of observed luminosities, consistent with the expected increase of L with time during the main sequence phase (see Sect. 8.3). The same can be said for the radii (right panel of Fig. 8.5), although the scatter in observed radii appears much larger. Partly this is due to the much finer scale of the ordinate in this diagram compared to the luminosity plot. The fact that most of the observed stellar radii are larger than the detailed ZAMS models is explained by expansion during (and after) the main sequence (see Sect. 8.3).

The location of the detailed ZAMS models in the H-R diagram is shown in Fig. 8.6. The solid (blue) line depicts models for quasi-solar composition, which were also used in Fig. 8.5. The increase of effective temperature with stellar mass (and luminosity) reflects the steep mass-luminosity relation and the much shallower mass-radius relation – more luminous stars with similar radii must be hotter, by eq. (1.1). The slope of the ZAMS in the HRD is not constant, reflecting non-homologous changes in structure as the stellar mass increases.

The effect of *composition* on the location of the ZAMS is illustrated by the dashed (red) line, which is computed for a metal-poor mixture characteristic of Population II stars. Metal-poor main sequence stars are hotter and have smaller radii. Furthermore, relatively low-mass stars are also more luminous than their metal-rich counterparts. One reason for these differences is a lower bound-free opacity at lower Z (eq. 4.33), which affects relatively low-mass stars (up to about $5\,M_\odot$). On the other hand, higher-mass stars are dominated by electron-scattering opacity, which is independent of metallicity. These stars are smaller and hotter for a different reason (see Sect. 8.2.1).

8.2.1 Central conditions

We can estimate how the central temperature and central density scale with mass and composition for a ZAMS star from the homology relations for homogeneous, radiative stars in thermal equilibrium (Sec. 6.4.2, see eqs. 6.37 and 6.38 and Table 6.1). From these relations we may expect the central

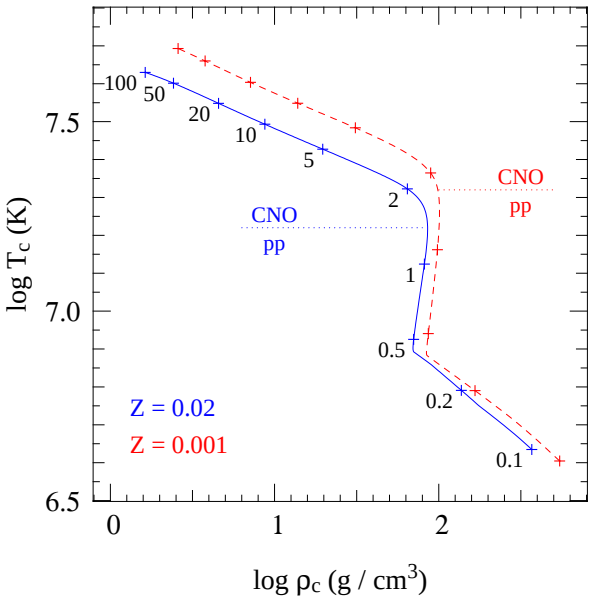

Figure 8.7. Central temperature versus central density for detailed ZAMS models with $X = 0.7, Z = 0.02$ (blue solid line) and with $X = 0.757, Z = 0.001$ (red dashed line). Plus symbols indicate models for specific masses (in units of $M_\odot$). The dotted lines indicate the approximate temperature border between energy production dominated by the CNO cycle and the pp chain. This gives rise to a change in slope of the T_c, ρ_c relation.

temperature to increase with mass, the mass dependence being larger for the pp chain ($T_c \propto M^{0.57}$) than for the CNO cycle ($T_c \propto M^{0.21}$). Since the CNO cycle dominates at high T, we can expect low-mass stars to power themselves by the pp chain and high-mass stars by the CNO cycle. This is confirmed by detailed ZAMS models, as shown in Fig. 8.7. For solar composition, the transition occurs at $T \approx 1.7 \times 10^7$ K, corresponding to $M \approx 1.3\,M_\odot$. Similarly, from the homology relations, the central density is expected to decrease strongly with mass in stars dominated by the CNO cycle ($\rho_c \propto M^{-1.4}$), but much less so in pp-dominated low-mass stars ($\rho_c \propto M^{-0.3}$). Also this is borne out by the detailed models in Fig. 8.7; in fact the central density increases slightly with mass between 0.4 and 1.5 $M_\odot$. The abrupt change in slope at 0.4 $M_\odot$ is related to the fact that stars with $M \lesssim 0.4\,M_\odot$ are completely convective. For these lowest-mass stars one of the main assumptions made in the homology relations (radiative equilibrium) breaks down.

The energy generation rate of the CNO cycle depends on the total CNO abundance. At lower metallicity, the transition between pp chain and CNO cycle therefore occurs at a higher temperature. As a consequence, the mass at which the transition occurs is also larger. Furthermore, high-mass stars powered by the CNO cycle need a higher central temperature to provide the same total nuclear power. Indeed, comparing metal-rich and metal-poor stars in Figs. 8.6 and 8.7, the luminosity of two stars with the same mass is similar, but their central temperature is higher. As a consequence of the virial theorem (eq. 2.27 or 6.28), their radius must be correspondingly smaller.

8.2.2 Convective regions

An overview of the occurrence of convective regions on the ZAMS as a function of stellar mass is shown in Fig. 8.8. For any given mass M, a vertical line in this diagram shows which conditions are encountered as a function of depth, characterized by the fractional mass coordinate m/M. Gray shading indicates whether a particular mass shell is convective or radiative (white). We can thus distinguish three types of ZAMS star:

- completely convective, for $M < 0.35\,M_\odot$,
- radiative core + convective envelope, for $0.35\,M_\odot < M < 1.2\,M_\odot$,
- convective core + radiative envelope, for $M > 1.2\,M_\odot$.

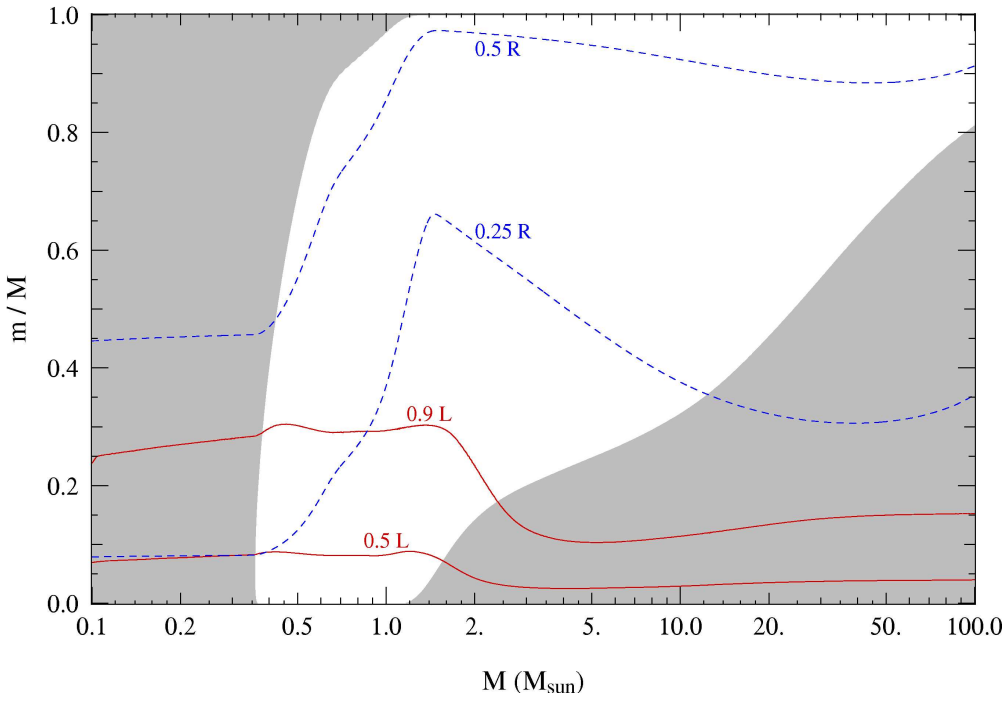

Figure 8.8. Occurrence of convective regions (gray shading) on the ZAMS in terms of fractional mass coordinate m/M as a function of stellar mass, for detailed stellar models with a composition $X = 0.70$, $Z = 0.02$. The solid (red) lines show the mass shells inside which 50% and 90% of the total luminosity are produced. The dashed (blue) lines show the mass coordinate where the radius r is 25% and 50% of the stellar radius R. (After Kippenhahn & Weigert.)

This behaviour can be understood from the Schwarzschild criterion for convection, which tells us that convection occurs when $\nabla_{\rm rad} > \nabla_{\rm ad}$ (eq. 4.50). As discussed in Sec. 4.5.1, a large value of $\nabla_{\rm rad}$ is found when the opacity κ is large, or when the energy flux to be transported (in particular the value of l/m) is large, or both. Starting with the latter condition, this is the case when a lot of energy is produced in a core of relatively small mass, i.e. when the energy generation rate $\epsilon_{\rm nuc}$ is strongly peaked towards the centre. This is certainly the case when the CNO-cycle dominates the energy production, since it is very temperature sensitive ($\nu \approx 18$) which means that $\epsilon_{\rm nuc}$ rapidly drops as the temperature decreases from the centre outwards. It results in a steep increase of $\nabla_{\rm rad}$ towards the centre and thus to a convective core. This is illustrated for a 4 $M_\odot$ ZAMS star in Fig. 4.5. The size of the convective core increases with stellar mass (Fig. 8.8), and it can encompass up to 80% of the mass of the star when M approaches 100 $M_\odot$. This is mainly related with the fact that at high mass, $\nabla_{\rm ad}$ is depressed below the ideal-gas value of 0.4 because of the growing importance of radiation pressure. At 100 $M_\odot$ radiation pressure dominates and $\nabla_{\rm ad} \approx 0.25$.

In low-mass stars the pp-chain dominates, which has a much smaller temperature sensitivity. Energy production is then distributed over a larger area, which keeps the energy flux and thus $\nabla_{\rm rad}$ low in the centre and the core remains radiative (see Fig. 4.5). The transition towards a more concentrated energy production at $M > 1.2\,M_\odot$ is demonstrated in Fig. 8.8 by the solid lines showing the location of the mass shell inside which most of the luminosity is generated.

Convective envelopes can be expected to occur in stars with low effective temperature, as discussed in Sec. 6.2.3. This is intimately related with the rise in opacity with decreasing temperature in the envelope. In the outer envelope of a 1 $M_\odot$ star for example, κ can reach values of 10^5 cm^2/g which results in enormous values of $\nabla_{\rm rad}$ (see Fig. 4.5). Thus the Schwarzschild criterion predicts a

convective outer envelope. This sets in for masses less than $\approx 1.5\,M_\odot$, although the amount of mass contained in the convective envelope is very small for masses between 1.2 and $1.5\,M_\odot$. Consistent with the discussion in Sec. 6.2.3, the depth of the convective envelope increases with decreasing $T_{\rm eff}$ and thus with decreasing M, until for $M < 0.35\,M_\odot$ the entire star is convective. Thus these very low-mass stars lie on their respective Hayashi lines.

8.3 Evolution during central hydrogen burning

Fig. 8.9 shows the location of the ZAMS in the H-R diagram and various evolution tracks for different masses at Population I composition, covering the central hydrogen burning phase. Stars evolve away from the ZAMS towards higher luminosities and larger radii. Low-mass stars ($M \lesssim 1\,M_\odot$) evolve towards higher $T_{\rm eff}$, and their radius increase is modest. Higher-mass stars, on the other hand, evolve towards lower $T_{\rm eff}$ and strongly increase in radius (by a factor 2 to 3). Evolved main-sequence stars are therefore expected to lie above and to the right of the ZAMS. This is indeed confirmed by comparing the evolution tracks to observed stars with accurately determined parameters.

As long as stars are powered by central hydrogen burning they remain in hydrostatic and thermal equilibrium. Since their structure is completely determined by the four (time-independent) structure equations, the evolution seen in the HRD is due to the changing composition inside the star (i.e. due to chemical evolution of the interior). How can we understand these changes?

Nuclear reactions on the MS have two important effects on the structure:

- Hydrogen is converted into helium, therefore the mean molecular weight μ increases in the core of the star (by more than a factor two from the initial H-He mixture to a pure He core by the end of central hydrogen burning). The increase in luminosity can therefore be understood from the homology relation $L \propto \mu^4\,M^3$. It turns out that the μ^4 dependence of this relation describes the luminosity increase during the MS quite well, if μ is taken as the mass-averaged value over the whole star.

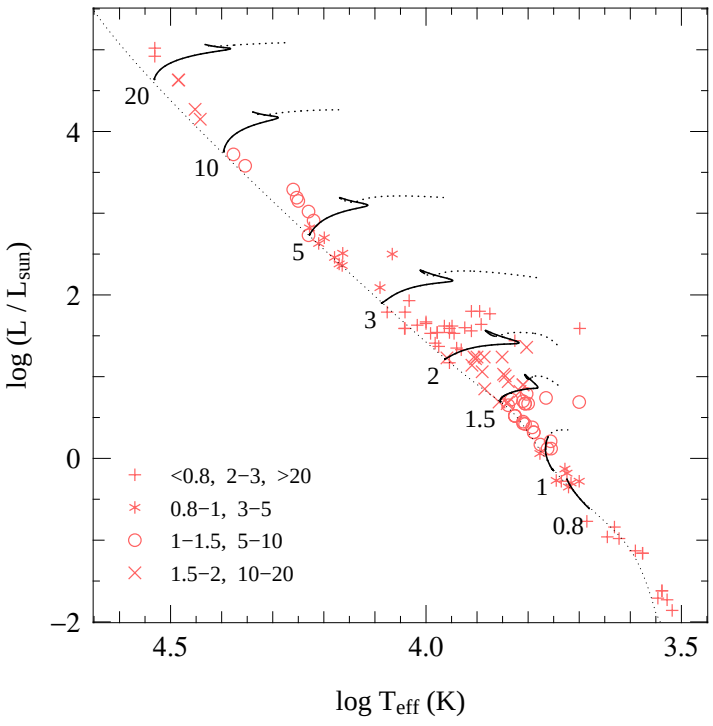

Figure 8.9. Evolution tracks in the H-R diagram during central hydrogen burning for stars of various masses, as labelled (in $M_\odot$), and for a composition $X = 0.7, Z = 0.02$. The dotted portion of each track shows the continuation of the evolution after central hydrogen exhaustion; the evolution of the $0.8\,M_\odot$ star is terminated at an age of 14 Gyr. The thin dotted line in the ZAMS. Symbols show the location of binary components with accurately measured mass, luminosity and radius (as in Fig. 8.5). Each symbol corresponds to a range of measured masses, as indicated in the lower left corner (mass values in $M_\odot$).

- The nuclear energy generation rate $\epsilon_{\rm nuc}$ is very sensitive to the temperature. Therefore nuclear reactions act like a *thermostat* on the central regions, keeping the central temperature almost constant. Since approximately $\epsilon_{\rm pp} \propto T^4$ and $\epsilon_{\rm CNO} \propto T^{18}$, the CNO cycle is a better thermostat than the pp chain. Since the luminosity increases and at the same time the hydrogen abundance decreases during central H-burning, the central temperature must increase somewhat to keep up the energy production, but the required increase in T_c is very small.

Since μ increases while $T_c \approx$ constant, the ideal-gas law implies that $P_c/\rho_c \propto T_c/\mu$ must decrease. This means that either the central density must increase, or the central pressure must decrease. The latter possibility means that the layers surrounding the core must expand, as explained below. In either case, the density contrast between the core and the envelope increases, so that evolution during central H-burning causes *non-homologous* changes to the structure.

8.3.1 Evolution of stars powered by the CNO cycle

We can understand why rather massive stars ($M \gtrsim 1.3\,M_\odot$) expand during the MS by considering the pressure that the outer layers exert on the core:

$$P_{\rm env} = \int_{m_c}^{M} \frac{Gm}{4\pi r^4} dm \tag{8.14}$$

Expansion of the envelope (increase in r of all mass shells) means a decrease in the envelope pressure on the core. This decrease in pressure is needed because of the sensitive thermostatic action of the CNO cycle, $\epsilon_{\rm CNO} \propto \rho\, T^{18}$, which allows only very small increases in T_c and ρ_c. Since μ_c increases as H being is burned into He, the ideal-gas law dictates that P_c must decrease. This is only possible if $P_{\rm env}$ decreases, i.e. the outer layers must expand to keep the star in HE ($\rho_{\rm env} \downarrow$ and $R \uparrow$). This self-regulating envelope expansion mechanism is the only way for the star to adapt itself to the composition changes in the core while maintaining both HE and TE.

Another important consequence of the temperature sensitivity the CNO cycle is the large concentration of $\epsilon_{\rm nuc}$ towards the centre. This gives rise to a large central $\nabla_{\rm rad} \propto l/m$ and hence to *convective cores*, which are mixed homogeneously ($X(m)$ = constant within the convective core mass $M_{\rm cc}$). This increases the amount of fuel available and therefore the lifetime of central hydrogen burning (see Fig. 8.10). In general $M_{\rm cc}$ decreases during the evolution, which is a consequence of the fact that $\nabla_{\rm rad} \propto \kappa$ and since $\kappa \propto 1 + X$ for the main opacity sources (see Sect. 4.3) the opacity in the core decreases as the He abundance goes up.

Towards the end of the main sequence phase, as X_c becomes very small, the thermostatic action of the CNO reactions diminishes and T_c has to increase substantially to keep up the energy production. When hydrogen is finally exhausted, this occurs within the whole convective core of mass $M_{\rm cc}$ and $\epsilon_{\rm nuc}$ decreases. The star now loses more energy at its surface than is produced in the centre, it gets out of thermal equilibrium and it will undergo an overall contraction. This occurs at the red point of the evolution tracks in Fig. 8.9, after which $T_{\rm eff}$ increases. At the blue point of the hook feature in the HRD, the core has contracted and heated up sufficiently that at the edge of the former convective core the temperature is high enough for the CNO cycle to ignite again in a shell around the helium core. This is the start of the *hydrogen-shell burning* phase which will be discussed in Chapter 9.

8.3.2 Evolution of stars powered by the pp chain

In stars with $M \lesssim 1.3\,M_\odot$ the central temperature is too low for the CNO cycle and the main energy-producing reactions are those of the pp chain. The lower temperature sensitivity $\epsilon_{\rm pp} \propto \rho\, T^4$ means that T_c and ρ_c increase more than was the case for the CNO cycle. Therefore the outer layers need to

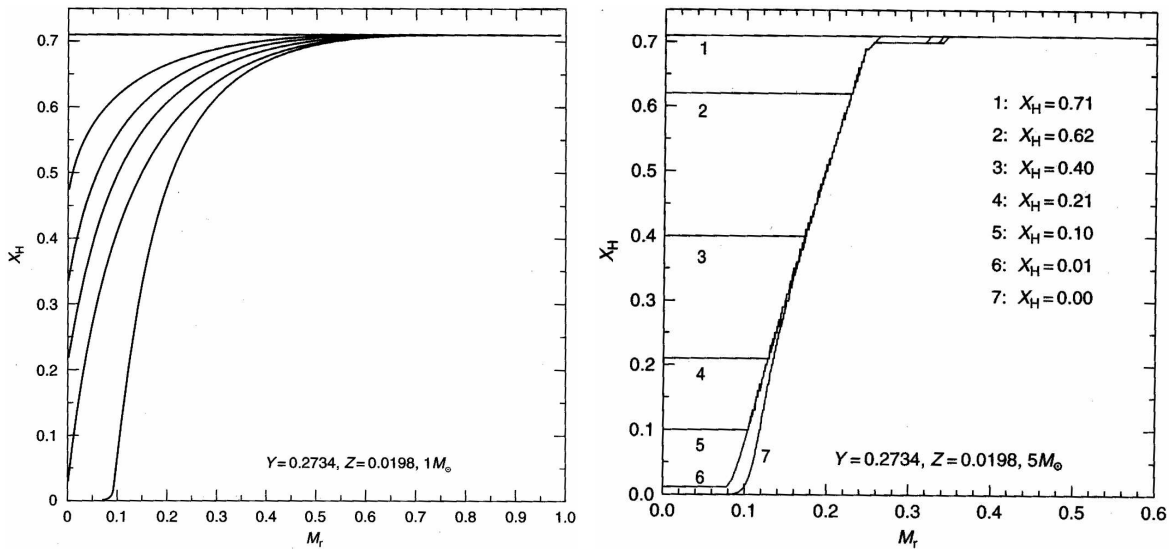

Figure 8.10. Hydrogen abundance profiles at different stages of evolution for a 1 $M_\odot$ star (left panel) and a 5 $M_\odot$ star (right panel) at quasi-solar composition. Figures reproduced from SALARIS & CASSISI.

expand less in order to maintain hydrostatic equilibrium in the core. As a result, the radius increase in low-mass stars is modest and they evolve almost parallel to the ZAMS in the H-R diagram (see Fig. 8.9).

Furthermore, the lower T-sensitivity of the pp chains means that low-mass stars have radiative cores. The rate of change of the hydrogen abundance in each shell is then proportional to the overall reaction rate of the pp chain (by eq. 5.4), and is therefore highest in the centre. Therefore a hydrogen abundance gradient builds up gradually, with $X(m)$ increasing outwards (see Fig. 8.10). As a result, hydrogen is depleted gradually in the core and there is a smooth transition to hydrogen-shell burning. The evolution tracks for low-mass stars therefore do not show a hook feature.

Note that stars in the approximate mass range $1.1 - 1.3\,M_\odot$ (at solar metallicity) undergo a transition from the pp chain to the CNO cycle as their central temperature increases. Therefore these stars at first have radiative cores and later develop a growing convective core. At the end of the MS phase such stars also show a hook feature in the HRD.

8.3.3 The main sequence lifetime

The timescale $\tau_{\rm MS}$ that a star spends on the main sequence is essentially the nuclear timescale for hydrogen burning, given by eq. (2.35). Another way of deriving essentially the same result is by realizing that, in the case of hydrogen burning, eq. (5.4) for the rate of change of the hydrogen abundance X and eq. (5.8) for the energy generation rate combine to

$$\frac{dX}{dt} = -\frac{4m_{\rm u}}{Q_{\rm H}}\,\epsilon_{\rm nuc}, \tag{8.15}$$

where $Q_{\rm H}$ is the effective energy release of the reaction chain ($4\,{}^1{\rm H} \rightarrow {}^4{\rm He} + 2\,{\rm e}^+ + 2\,\nu$), i.e. corrected for the neutrino losses. Hence $Q_{\rm H}$ is somewhat different for the pp chain and the CNO cycle. Note that $Q_{\rm H}/(4m_{\rm u}c^2)$ corresponds to the factor ϕ used in eq. (2.35). If we integrate eq. (8.15) over all mass shells we obtain, for a star in thermal equilibrium,

$$\frac{dM_{\rm H}}{dt} = -\frac{4m_{\rm u}}{Q_{\rm H}}\,L. \tag{8.16}$$

Here $M_{\rm H}$ is the total mass of hydrogen in the star. Note that while eq. (8.15) only strictly applies to regions where there is no mixing, eq (8.16) is also valid if the star has a convective core, because convective mixing only redistributes the hydrogen supply. If we now integrate over the main sequence lifetime we obtain for the total mass of hydrogen consumed

$$\Delta M_{\rm H} = \frac{4m_{\rm u}}{Q_{\rm H}} \int_0^{\tau_{\rm MS}} L\, dt = \frac{4m_{\rm u}}{Q_{\rm H}} \bar{L} \cdot \tau_{\rm MS}, \tag{8.17}$$

where $\bar{L}$ is the time average of the luminosity over the main-sequence lifetime. We can write $\Delta M_{\rm H} = f_{\rm nuc} M$ by analogy with eq. (2.35), and write $f_{\rm nuc}$ as the product of the initial hydrogen mass fraction X_0 and an effective core mass fraction $q_{\rm c}$ inside which all hydrogen is consumed, so that

$$\tau_{\rm MS} = X_0 q_{\rm c} \frac{Q_{\rm H}}{4m_{\rm u}} \frac{M}{\bar{L}}. \tag{8.18}$$

We have seen that the luminosity of main-sequence stars increases strongly with mass. Since the variation of L during the MS phase is modest, we can assume the same relation between $\bar{L}$ and M as for the ZAMS. The other factors appearing in eq. (8.18) do not or only weakly depend on the mass of the star (see below) and can in a first approximation be taken as constant. For a mass-luminosity relation $\bar{L} \propto M^{\eta}$ – where η depends on the mass range under consideration with $\eta \approx 3.8$ on average – we thus obtain $\tau_{\rm MS} \propto M^{1-\eta}$. Hence $\tau_{\rm MS}$ decreases strongly towards larger masses.

This general trend has important consequences for the observed H-R diagrams of star clusters. All stars in a cluster can be assumed to have formed at approximately the same time and therefore now have the same age $\tau_{\rm cl}$. Cluster stars with a mass above a certain limit $M_{\rm to}$ have main-sequence lifetimes $\tau_{\rm MS} < \tau_{\rm cl}$ and have therefore already left the main sequence, while those with $M < M_{\rm to}$ are still on the main sequence. The main sequence of a cluster has an upper end (the 'turn-off point') at a luminosity and effective temperature corresponding to $M_{\rm to}$, the so-called *turn-off mass*, determined by the condition $\tau_{\rm MS}(M_{\rm to}) = \tau_{\rm cl}$. The turn-off mass and luminosity decrease with cluster age (e.g. see Fig. 1.2). This the basis for the *age determination* of star clusters.

The actual main-sequence lifetime depend on a number of other factors. The effective energy release $Q_{\rm H}$ depends on which reactions are involved in energy production and therefore has a slight mass dependence. More importantly, the exact value of $q_{\rm c}$ is determined by the hydrogen profile left at the end of the main sequence. This is somewhat mass-dependent, especially for massive stars in which the relative size of the convective core tends to increase with mass (Fig. 8.8). A larger convective core mass means a larger fuel reservoir and a longer lifetime. Our poor understanding of convection and mixing in stars unfortunately introduces considerable uncertainty in the size of this reservoir and therefore both in the main-sequence lifetime of a star of a particular mass and in its further evolution.

8.3.4 Complications: convective overshooting and semi-convection

As discussed in Sect. 4.5.4, the size of a convective region inside a star is expected to be larger than predicted by the Schwarzschild (or Ledoux) criterion because of convective *overshooting*. However, the extent $d_{\rm ov}$ of the overshooting region is not known reliably from theory. In stellar evolution calculations this is usually parameterized in terms of the local pressure scale height, $d_{\rm ov} = \alpha_{\rm ov} H_P$. In addition, other physical effects such as stellar rotation may contribute to mixing material beyond the formal convective core boundary. Detailed stellar evolution models in which the effects of convective overshooting are taken into account generally provide a better match to observations. For this reason, overshooting (or perhaps a variety of enhanced mixing processes) is thought to have a significant effect in stars with sizable convective cores on the main sequence.

Overshooting has several important consequences for the evolution of a star:

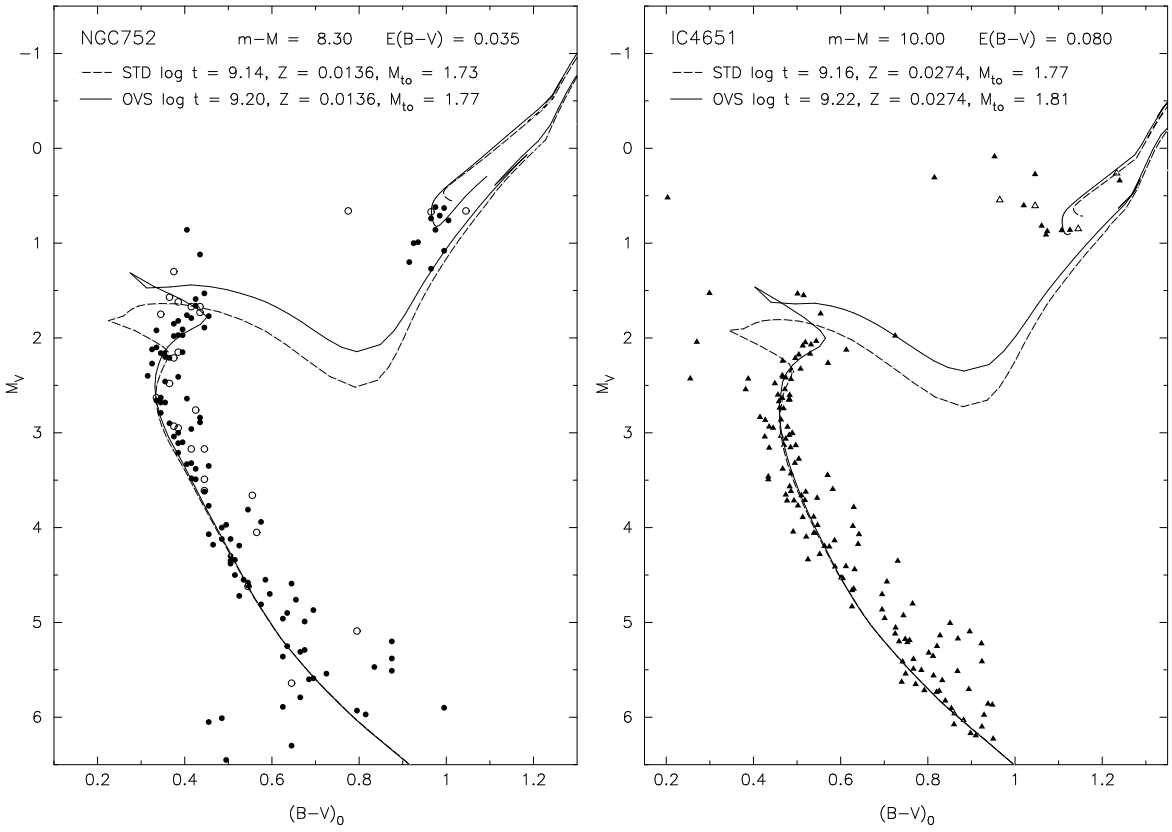

Figure 8.11. Two examples of *isochrone fitting* to the colour-magnitude diagrams of open clusters, NGC 752 and IC 4651. The distribution of stars in the turn-off region is matched to isochrones for standard stellar evolution models (STD) and for models with convective overshooting (OVS). The overshooting models are better able to reproduce the upper extension of the main sequence band in both cases.

1. a longer main-sequence lifetime, because of the larger hydrogen reservoir available;
2. a larger increase in luminosity and radius during the main sequence, because of the larger region inside which μ increases which enhances the effects on L and R discussed earlier in this section;
3. the hydrogen-exhausted core mass is larger at the end of the main sequence, which in turn leads to (a) larger luminosities during all evolution phases after the main sequence and, as a result, (b) *shorter* lifetimes of these post-main sequence phases.

Some of these effects, particularly (2) and (3a), provide the basis of observational tests of overshooting. Stellar evolution models computed with different values of $\alpha_{\rm ov}$ are compared to the observed width of the main sequence band in star clusters (see for example Fig. 8.11), and to the luminosities of evolved stars in binary systems. If the location in the HRD of the main sequence turn-off in a cluster is well determined, or if the luminosity difference between binary components can be accurately measured, a quantitative test is possible which allows a calibration of the parameter $\alpha_{\rm ov}$. Such tests indicate that $\alpha_{\rm ov} \approx 0.25$ is appropriate in the mass range $1.5 - 8\,M_\odot$. For larger masses, however, $\alpha_{\rm ov}$ is poorly constrained.

Another phenomenon that introduces an uncertainty in stellar evolution models is related to the difference between the Ledoux and Schwarzschild criterion for convection (see Sect. 4.5.1). Outside the convective core a composition gradient (∇_μ) develops, which can make this region dynamically stable according to the Ledoux criterion while it would have been convective if the Schwarzschild

criterion were applied. In such a region an overstable oscillation pattern can develop on the thermal timescale, which slowly mixes the region and thereby smooths out the composition gradient. This process is called *semi-convection*. Its efficiency and the precise outcome are uncertain. Semi-convective situations are encountered during various phases of evolution, most importantly during central hydrogen burning in stars with $M > 10\,M_\odot$ and during helium burning in low- and intermediate-mass stars.

Suggestions for further reading

The process of star formation and pre-main sequence evolution is treated in much more detail in Chapters 18–20 of Maeder, while the properties and evolution on the main sequence are treated in Chapter 25. See also Kippenhahn & Weigert Chapters 22 and 26–30.

Exercises

8.1 Kippenhahn diagram of the ZAMS

Figure 8.8 indicates which regions in zero-age main sequence stars are convective as function for stars with different masses.

(a) Why are the lowest-mass stars fully convective? Why does the mass of the convective envelope decrease with M and disappear for $M \gtrsim 1.3 M_\odot$?

(b) What changes occur in the central energy production around M = 1.3 $M_\odot$, and why? How is this related to the convection criterion? So why do stars with $M \approx 1.3 M_\odot$ have convective cores while lower-mass stars do not?

(c) Why is it plausible that the mass of the convective core increases with M?

8.2 Conceptual questions

(a) What is the Hayashi line? Why is it a line, in other words: why is there a whole range of possible luminosities for a star of a certain mass on the HL?

(b) Why do no stars exist with a temperature cooler than that of the HL? What happens if a star would cross over to the cool side of the HL?

(c) Why is there a mass-luminosity relation for ZAMS stars? (In other words, why is there a unique luminosity for a star of a certain mass?)

(d) What determines the shape of the ZAMS is the HR diagram?

8.3 Central temperature versus mass

Use the homology relations for the luminosity and temperature of a star to derive how the central temperature in a star scales with mass, and find the dependence of T_c on M for the pp-chain and for the CNO-cycle. To make the result quantitative, use the fact that in the Sun with $T_c \approx 1.3 \times 10^7$,K the pp-chain dominates, and that the CNO-cycle dominates for masses $M \gtrsim 1.3 M_\odot$. (Why does the pp-chain dominate at low mass and the CNO-cycle at high mass?)

8.4 Mass-luminosity relation

Find the relation between L and M and the slope of the main sequence, assuming an opacity law $\kappa = \kappa_0 \rho T^{-7/2}$ (the Kramers opacity law) and that the energy generation rate per unit mass $\epsilon_{nuc} \propto \rho T^\nu$, where $\nu = 4$.